Hindawi
Advances in Materials Science and Engineering
Volume 2021, Article ID 6678280, 16 pages
https://doi.org/10.1155/2021/6678280

Research Article

Spheroidization and Coarsening of Eutectic Si Particles in Al-Si-Based Alloys

Mohamed Ibrahim,[1] Mohamed Abdelaziz,[2] Agnes Samuel,[1] Herbert Doty,[3] and Fawzy Samuel[1]

[1]*Université du Québec à Chicoutimi, Saguenay, Québec, Canada*
[2]*Département PEC, Université Française d'Égypte, El Shorouk, Cairo, Egypt*
[3]*General Motors Materials Engineering, Pontiac, MI, USA*

Correspondence should be addressed to Fawzy Samuel; fhsamuel@uqac.ca

Received 23 November 2020; Revised 24 December 2020; Accepted 6 January 2021; Published 19 January 2021

Academic Editor: Gianfranco Carotenuto

The present study was carried out on three Al-Si cast alloys viz., 319, 356, and 413 alloys, solidified at 8°C/s. Samples from 319 and 413 alloys were solution heat-treated at 510°C, whereas samples from 356 alloy were solutionized at 550°C, for up to 1200 h. The results reveal that complete spheroidization of eutectic Si particles in terms of achieving individual spherical particles cannot be achieved in most Al-Si-Cu-Mg alloys even after a solutionizing time of 1200 h which contradicts with the existing theory. Addition of Sr to Cu-free 356 alloy could lead to complete spheroidization after 1200 h at 550°C if the alloy was solidified at 8°C/s. Besides the dissolution theory of Ostwald, coarsening of Si particles can as well take place by impingement, fusion, and agglomeration. Increasing the Si content makes it difficult to achieve spheroidization, i.e., fragmentation and coarsening. Results obtained from observations of deeply etched samples (3D) contradict those obtained from polished samples (2D).

1. Introduction

William Ostwald [1, 2] suggested the dissolution of small crystals or solid particles and the redeposition of the dissolved species on the surfaces of larger crystals or solid particles. The ripening process occurs because larger particles are more energetically favored than smaller particles, giving rise to an apparent higher solubility for the smaller ones [3] as schematically shown in Figure 1.

In the case of unmodified Al-Si alloys (for the majority of alloys), coarsening of Si particles takes place by a combination of particle fragmentation mechanism along with the silicon particle dilution mechanism, similar to that proposed by Ostwald. Smaller silicon particles dilute and diffuse to cause some silicon particles to grow laterally as presented in Figure 2 [4].

In nonmodified Al-Si-Mg alloys, the coarsening rate of eutectic silicon was found to follow the Lifshitz–Slyozof–Wagner (LSW) theory, which corresponds to a zero volume fraction approximation. The LSW model takes place after an initial time delay during which the fragmentation of the silicon plates takes place [5, 6]. The coarsening rate can be calculated using equation (1) following the diffusion-controlled growth model [7, 8], also known as the LSW model:

$$\overline{r}^3 - \overline{r_0}^3 = K_{\mathrm{LSW}} * t, \tag{1}$$

where $\overline{r}^3$ denotes the final average radius, $\overline{r_0}^3$ is the average radius at time $(t) = 0$, and K_{LSW} is the coarsening rate constant.

Colley [9] suggested that the roundness relates to the sharpness or smoothness of the particle's corners or edges, whereas the sphericity (or circularity) determines how the overall shape of the particles approaches that of a sphere (3D) or a circle (2D).

The equivalent circular diameter is the diameter of a circle that has the same area (A) as the Si particle and may be calculated using the following formula (Figure 3):

$$\text{equivalent circular diameter } (d) = \sqrt{\frac{4 * \text{particle area } (A)}{\pi}}. \tag{2}$$

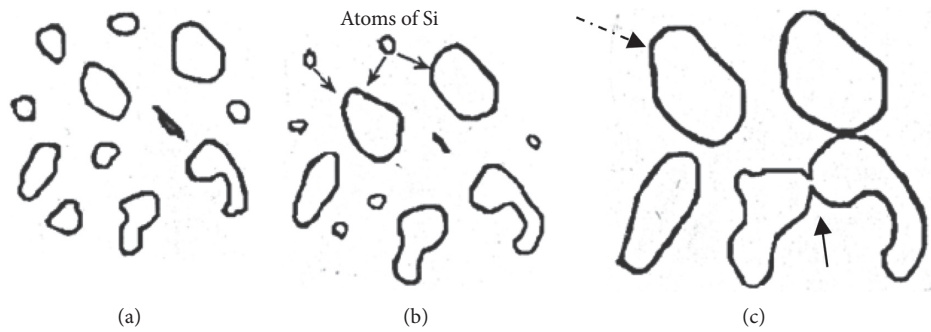

Figure 1: Schematization of the Ostwald dissolution mechanism: (a) before solutionizing; (b) dissolving of the small particles; (c) the large particles growing due to dissolution of the small ones (broken arrow) and/or by merging (black arrow) [3].

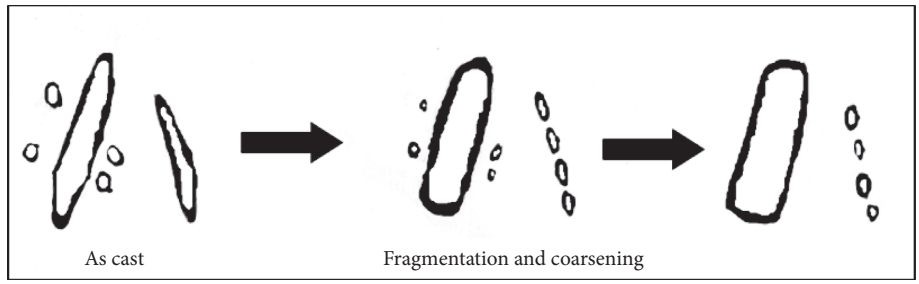

Figure 2: Schematic presentation of the new mechanism for the development of eutectic silicon particles during solution heat treatment [4].

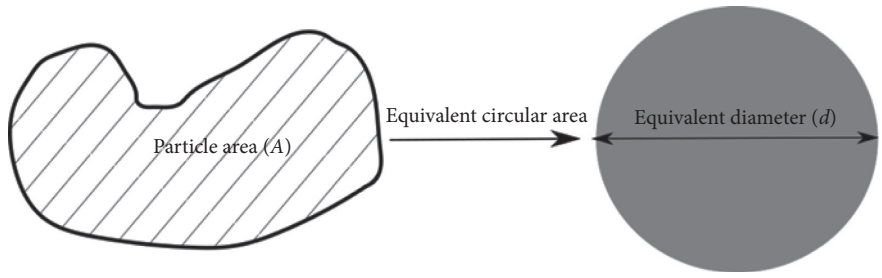

Figure 3: Schematic representation showing the projection of the Si particle as the equivalent circle with the same area A and the equivalent circular diameter d.

The aspect ratio of the particle is calculated by drawing an imaginary best fit ellipse to the particle projection; by measuring the major and minor axes of the ellipse, the aspect ratio can be calculated according to the following relation:

$$\text{aspect ratio } (A.R.) = \frac{\text{major axis length } (L)}{\text{minor axis length } (B)}. \quad (3)$$

The sphericity or circularity of the Si particles is a function of the perimeter (P) and the particle area (A); its value lies between 0 and 1, where the maximum value of 1 refers to a perfect circle. The sphericity is quantified as follows:

$$\text{sphericity} = \frac{4 * \pi * \text{particle area } (A)}{\text{Perimeter } (P)^2}. \quad (4)$$

Finally, the roundness of the particle's edges is a function of the particle area (A) and the length of the best fit ellipse major axis (L) and is given by:

$$\text{roundness} = \frac{4 * \text{particle area } (A)}{\pi * \text{major axis length } (L)^2}. \quad (5)$$

In the case of modified Al-Si alloys, prior to heat treatment, the addition of Sr changes or "modifies" the acicular morphology to a fine, fibrous form. Later, solution heat treatment (SHT) helps in spheroidizing the eutectic silicon in either nonmodified or modified alloys [10] (Figure 4). The change in the eutectic Si morphology occurs in two stages: (i) dissolution or fragmentation of the eutectic Si branches after necking and (ii) granulation or spheroidization of the fragmented branches as their average size

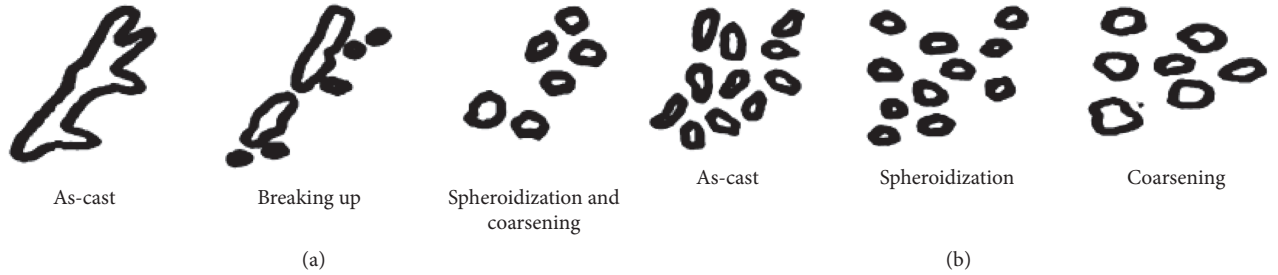

Figure 4: Schematic diagram showing the change of eutectic Si particle morphology during solution heat treatment in (a) nonmodified and (b) modified Al-Si cast alloys [14].

decreases, allowing eventual spheroidization. Many authors [11, 12] have stated that fragmentation of acicular silicon is facilitated by previous Sr treatment so that the resulting fibrous eutectic silicon would be spheroidized in a shorter time; this behavior was attributed to the larger interfacial area of the fibrous structure and driving force for morphological change [6, 13, 14]. On the other hand, nonmodified structures will take a longer time to be spheroidized. Figure 4 shows the sequence of spheroidization of the eutectic silicon particles in both nonmodified and modified Al-Si alloys [5, 6, 15, 16].

The processes of spheroidization and coarsening of eutectic silicon particles result mainly from the reduction in the surface energy associated with the interface between the silicon particles and the Al matrix [13, 17–21]. At elevated temperatures, the size and frequency of surface perturbations increase at the interface, leading to the formation of near-spherical Si particles due to the breakdown of the eutectic silicon particles. Subsequently, these near-spherical particles tend to coarsen to further reduce the interfacial area; the coarsening occurs by the dissolution of the smaller Si particles into the larger (more stable) particles following the Ostwald ripening mechanism.

Ogris et al. [17] studied the fragmentation of eutectic silicon rods into spheres in the Al-Si-Mg alloy by considering the model shown in Figure 5, where the cylindrical rod in the top half of the model represents the interconnected modified silicon particles. The authors concluded that the fragmentation time for eutectic silicon rods during solution treatment is highly dependent on the initial rod radius and the solutionizing temperature.

The main objective of the present work is to examine the abovementioned theories in Al-Si-Mg and Al-Si-Cu-Mg alloys using polished (2D) as well as deeply etched (3D) samples (solidified at 8°C/s) subjected to solutionizing time of up to 1200 h at different solutionizing temperatures.

2. Experimental Procedure

The as-received 354 alloy ingots were cut, dried, and melted in a 70 kg capacity SiC crucible using an electric resistance furnace. The Sr-modified alloy series was obtained by adding ~200 ppm Sr using Al-10 wt.% Sr master alloy, whereas the grain refinement was accomplished through the addition of Al-5 wt.% Ti-1 wt.% B master alloy in the form of rods in order to achieve a level of ~0.2 wt.% Ti in the final alloys. The melt was kept at a temperature of 800 ± 5°C. The degassing process was carried out using a rotary graphite impeller that rotates at ~150 rpm for 15–20 min; pure dry argon was pumped inside the melt through the rotating impeller at a constant rate of 20 m^3/h. It should be mentioned here that Sr was added 5 min before the end of degassing to minimize its oxidation. After degassing, the melt was carefully skimmed to remove the oxide layers from the melt surface. The melt was then poured into the 2 preheated permanent molds. Each permanent mold preheated at 450°C employed was preheated in order to remove all traces of moisture from the mold. An ASTM B-108-type permanent mold was used to prepare castings from which the standard tensile test bars were obtained (Figure 6(a)). The rest of the molten alloys were poured into a metallic mold heated at 350°C (Figure 6(b)) [22]. The solidification rate was ~8°C/s in both cases. Table 1 lists the chemical composition of the three alloys used in the present work.

Tensile testing at the ambient temperature was carried out using an MTS servo-hydraulic mechanical testing machine at a strain rate of $4 \times 10^{-4} \cdot s^{-1}$, for the as-cast and heat-treated test bars. The attachable extensometer (strain gauge) was used to measure the deformation that takes place in the samples during the test, and the data acquisition system attached to the machine converts it to an accurate measure of the percentage elongation. The data acquisition system provides the tensile properties in terms of ultimate tensile strength (UTS), yield strength (YS), and percentage elongation to fracture (%El). Five test bars for each alloy/condition were tested, and the average values of ultimate tensile strength (UTS), 0.2% offset yield strength (YS), and percentage elongation to fracture (%El) were reported to represent the tensile properties of the corresponding alloy/condition.

Samples for metallographic examination were sectioned from the cast bars (25 mm × 25 mm × 5 mm) and polished following standard procedures. Eutectic Si characteristics were evaluated using a Clemex image analyzer coupled with an optical microscope. Measurements were carried out at 100x as shown in Figure 7. For each sample, at least 100 fields were scanned to enhance the accuracy of the measurements. In order to better understand and visualize the morphological changes occurring in the silicon particles during extended solution treatment, the samples were deep etched using Keller's etchant to dissolve the aluminum matrix and expose the eutectic silicon particles. These samples were then

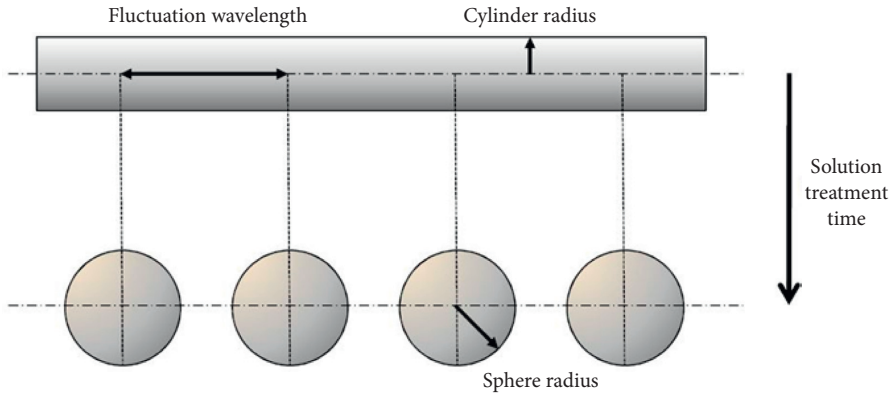

Figure 5: Schematic illustrating a rod-shaped eutectic particle that fragments into a series of spherical particles [17].

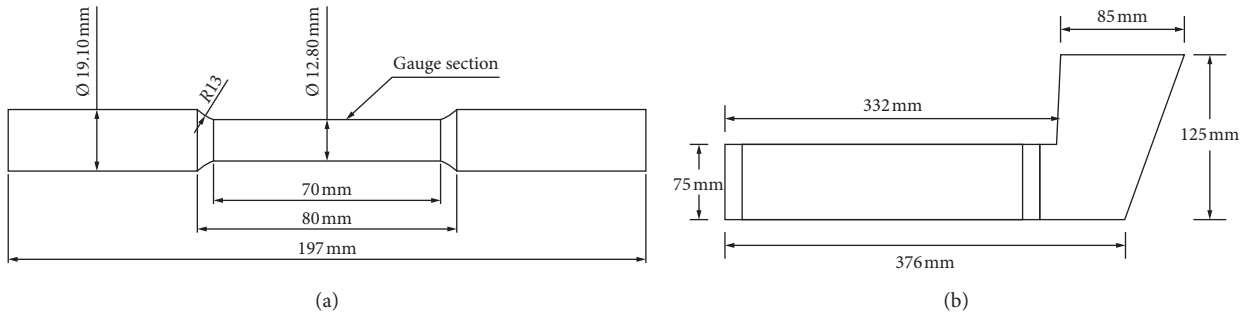

Figure 6: (a) Geometry of the standard tensile test bar obtained from ASTM B-108 permanent mold. (b) Schematic of the *L*-shaped mold used in the present study [22].

Table 1: Chemical composition (wt.%) of the alloys used in the present work.

Alloy	Cu	Mg	Mn	Si	Fe	Sr	Ti	B	SHT (°C)
319	3.1	0.0071	0.0005	5.6	0.17	0.0000	0.105	0.0004	510
356	0.06	0.314	0.0005	6.2	0.10	0.0001	0.0002	0.0002	550
413	1.2	0.046	0.218	11.2	0.34	0.0000	0.0652	0.0003	510

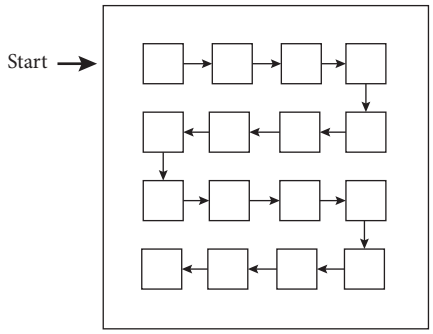

Figure 7: Schematic distribution of the examined fields.

examined by a Hitachi-SU8000 field-emission scanning electron microscope (FESEM) using the backscattered electron (BSE) mode.

3. Results and Discussion

3.1. Image Analysis Results. A study of Tables 2–5 shows that the average surface area of the silicon particles of alloy 319 increases with solutionizing treatment, both for modified and unmodified samples. Thus, there is a growth of the thickness of the silicon particles which may be accompanied by an increase in length for the unmodified samples. For Sr-modified samples, the silicon particles undergo fragmentation, followed by coarsening. Thus, particle density is increased in these samples. Solution heat treatment has the effect of reducing the density of the Si particles in the samples. Therefore, there is dissolution of certain silicon particles which feed the growth of other silicon particles. Roundness is higher for samples that contain strontium (62.6% in amount). Roundness for such samples also increases with SHT. In the case of high Si-containing alloy, i.e.,

413 alloy, the rate of fragmentation of silicon particles is lower compared to that observed for 319 and 356 alloys, which allows for an increase in the thickness of the silicon particles, to maintain or increase the surface area of the particles. As in the case of other alloys, roundness, for samples containing strontium, also increases with SHT (76.6% in amount).

3.2. Optical Microstructure. Figures 8–10 represent the microstructure of the present alloys under different working conditions. Figure 8(a) shows the typical microstructure of a 319 alloy before SHT, which is composed of needle-like eutectic silicon and eutectic $CuAl_2$ precipitates. After SHT (Figure 8(b)), it is observed that there is a dissolution of the $CuAl_2$ precipitates (black arrows) [23, 24] and the fine silicon particles are observed within the latter. There is also an increase in the thickness and length of the needle-like silicon particles. The circle in Figure 8(b) reveals the fragmentation of a silicon particle. The inset in this figure reveals the presence of ultrafine Si particles within the Al-$CuAl_2$ eutectic indicating the end of solidification. Figures 8(c) and 8(d) depict the microstructures of the Sr-modified samples, before and after SHT for 24 h at 510°C, respectively. As can be seen, the addition of Sr allows for almost complete dissolution of the $CuAl_2$ phase during the SHT process. A comparison between Figures 9(a) and 9(b) clearly demonstrates the thickening of the Si particles following solutionizing for 24 h at 550°C (a temperature that is 40°C above that used for 319 and 413 alloys).

The microstructure of alloy 413 before SHT is shown in Figure 10(a). It is composed of primary silicon, eutectic silicon, and the α-$Al_{15}(Mn,Fe)_3Si_2$ intermetallic phase (Chinese script). The latter is obtained due to the presence of elements such as Mn and Cr. These Chinese script particles, in unmodified alloys, are found between the particles of eutectic silicon. Solutionizing the as-cast alloy at 510°C for 24 h, Figure 10(b), caused an increase in the thickness and length of the silicon particles. Another observation that can be made for these samples is that the addition of strontium causes a shift in the Al-Si eutectic point, leading to the disappearance of the primary silicon particles. The Sr-modified sample, after SHT (Figure 10(d)), confirms the presence of the α-$Al_{15}(Mn,Fe)_3Si_2$ intermetallic inside the α-aluminum dendrites (black arrows) [20]. Apparently, solution heat treatment of the sample (Figure 10(d)) has no effect on the size of the silicon particles.

3.3. Etched Samples. According to Fick's first law [25], atoms throughout the solid are constantly vibrating from thermal energy. At a given temperature, each atom in the slice has a frequency at which it will jump to the adjacent slice, ν with equal probability of jumping in either direction; therefore, the frequency of jump from one slice to the next in a particular direction is $\nu/2$ (Figure 11(a)). Whether an impurity atom occupies a substitutional or interstitial position, the atom is trapped in a periodic potential defined by the lattice. The probability of an atom jumping from one position to the next increases exponentially with the increasing temperature (Figure 11(b)) [26].

LeClaire and Lidiard [27] proposed a model to explain impurity-diffusion in the fcc system as shown in Figure 12.

Figure 13 presents the variation in the size and distribution of the Si particles as a function of heating at 550°C for different solutionizing times. As can be seen, in the nonmodified condition, the eutectic Si precipitated in the form of thin platelets with sharp angles (white circle in Figure 13(a)). Fragmentation was observed after 24 h, Figure 13(b) similar to that depicted in Figure 8(b) and continued with the increase in heating time up to 100 h (see Figure 13(c)) (see arrows), with traces of fragmentation after 400 h-white arrows in Figure 13(d). Figure 13(e) is a high-magnification electron image of Figure 13(d) revealing the clustering of several small platelets in order to form one particle. Partial spheroidization was observed after 1200 h solutionizing at 550°C as displayed in Figure 13(f). Note the elongated shape of some particles (white arrow).

The addition of 200 ppm Sr to the 356 alloy resulted in complete modification as demonstrated in Figure 14(a) with faster fragmentation after 24 h (arrowed) (Figure 14(b)), compared to that observed in the case of nonmodified alloy. Unlike what was seen in the optical micrographs, the Si particles are not individual. Prolonged solutionizing at 550°C resulted in more clustering of the Si particles (white circles in Figures 14(c) and 14(d)) with partial spheriodization achieved after 400 h. The formation of these clusters explains the large standard deviations reported in Tables 2–5. Solutionizing for 1200 h led to practically spherical particles (Figure 14(f)). It should be kept in mind that the addition of Sr depresses the eutectic temperature coupled with a shift in the eutectic point to a higher Si content [28].

In the case of 413 alloy that contains 11.7% Si, the rates of fragmentation and coarsening are expected to be much slower than those exhibited by 356 alloy. In addition, the maximum solutionizing temperature is about 510°C compared to 550°C for the 356 alloy. Figure 15 depicts the variation in the Si particle morphology and size with the applied heat treatment. After 1200 h, the unmodified alloy still showed elongated particles (see white arrow in Figure 15(c)), with more spheroidization in the modified alloy (Figure 15(d)). Increasing the solutionizing temperature to 565°C resulted in incipient melting in both 356 and 413 alloys even after a short solutionizing time of 8 h as shown in Figure 16 [29].

Based on intensive SEM examination of all conditions, it seems that there is more than one mechanism for Si particle coarsening as illustrated in Figure 17, before reaching the same microstructure viewed by the optical microscope. Most of the Si particles show the presence of pinholes (broken arrows in Figure 17(f)) that go through the entire particle (broken arrow in Figure 17(e)) or conical cavities (solid arrow in Figure 17(e)) which may need further sectioning to reveal their cause.

3.4. Applications. The ambient-temperature tensile properties of 356-type alloys solutionized up to 400 h are plotted in Figure 18(a) (nonmodified) and Figure 18(b) (Sr-modified) [22]. Both alloys show the same trend in strength variation for

Table 2: Characteristics of Si particles in 319 alloy (coded A) at different conditions (nonmodified).

Condition	Average particle area (μm^2)		Average particle length (μm)		Particle roundness (%)		Particle aspect ratio		Density (particles/μm^2)
	μ^*	σ^{**}	μ	Σ	M	σ	μ	σ	μ
As-cast	48.99	18.19	13.26	6.89	67.10	32.36	2.55	1.52	2365
8 h@510°C	86.55	49.69	15.63	13.04	60.87	31.94	2.48	1.42	1762
24 h@510°C	75.86	52.51	14.66	13.47	60.23	29.49	2.42	1.34	1455

*Average value; **standard deviation.

Table 3: Characteristics of Si particles in 319 alloy (coded A) at different conditions (Sr-modified).

Condition	Average particle area (μm^2)		Average particle length (μm)		Particle roundness (%)		Particle aspect ratio		Density (particles/μm^2)
	M	σ	μ	Σ	μ	σ	μ	σ	μ
As-cast	3.61	8.48	2.79	2.91	74.67	23.75	1.91	0,73	15212
8 h@510°C	6.71	12.75	3.54	3.31	81.25	18.81	1.71	0.66	10679
24 h@510°C	11.71	18.46	5.04	4.58	70.97	24.76	1.89	0.83	6492

Table 4: Characteristics of Si particles in 356 alloy at different conditions (nonmodified (coded B) and Sr-modified (coded BS) conditions).

Alloy code	Solutionizing time (h)	Particle area (μm^2)	Sphericity (%)	Roundness (%)	Aspect ratio	Density (particles/mm^2)
B	As-cast	$\mu^* = 14.30$ $\sigma^{**} = 11.70$	$\mu = 41.60$ $\sigma = 22.70$	$\mu = 36.30$ $\sigma = 19.00$	$\mu = 2.44$ $\sigma = 1.53$	$\mu = 27000$
	8	$\mu = 21.50$ $\sigma = 17.30$	$\mu = 72.50$ $\sigma = 18.00$	$\mu = 46.30$ $\sigma = 17.70$	$\mu = 1.83$ $\sigma = 1.53$	$\mu = 1200$
	24	$\mu = 27.50$ $\sigma = 19.30$	$\mu = 42.50$ $\sigma = 18.00$	$\mu = 50.30$ $\sigma = 17.70$	$\mu = 1.63$ $\sigma = 1.50$	$\mu = 4200$
	50	$\mu = 33.70$ $\sigma = 22.80$	$\mu = 72.90$ $\sigma = 16.30$	$\mu = 56.40$ $\sigma = 16.90$	$\mu = 1.73$ $\sigma = 0.81$	$\mu = 7000$
	100	$\mu = 48.00$ $\sigma = 48.70$	$\mu = 78.20$ $\sigma = 18.10$	$\mu = 64.90$ $\sigma = 24.20$	$\mu = 1.78$ $\sigma = 0.98$	$\mu = 3500$
	200	$\mu = 69.10$ $\sigma = 44.10$	$\mu = 79.20$ $\sigma = 18.30$	$\mu = 63.80$ $\sigma = 24.10$	$\mu = 1.79$ $\sigma = 1.12$	$\mu = 2700$
	400	$\mu = 77.60$ $\sigma = 63.70$	$\mu = 81.00$ $\sigma = 18.80$	$\mu = 66.80$ $\sigma = 22.70$	$\mu = 1.71$ $\sigma = 1.15$	$\mu = 3100$
	1200	$\mu = 85.60$ $\sigma = 45.70$	$\mu = 87.00$ $\sigma = 15.80$	$\mu = 69.80$ $\sigma = 22.70$	$\mu = 1.51$ $\sigma = 1.15$	$\mu = 3900$
BS	As-cast	$\mu = 6.82$ $\sigma = 6.05$	$\mu = 54.90$ $\sigma = 23.20$	$\mu = 46.30$ $\sigma = 17.50$	$\mu = 1.88$ $\sigma = 0.81$	$\mu = 44000$
	8	$\mu = 15.30$ $\sigma = 11.60$	$\mu = 75.50$ $\sigma = 17.40$	$\mu = 62.20$ $\sigma = 15.20$	$\mu = 1.53$ $\sigma = 0.56$	$\mu = 17000$
	24	$\mu = 21.30$ $\sigma = 15.60$	$\mu = 76.50$ $\sigma = 17.40$	$\mu = 63.20$ $\sigma = 14.70$	$\mu = 1.00$ $\sigma = 0.56$	$\mu = 4350$
	50	$\mu = 28.40$ $\sigma = 20.90$	$\mu = 78.30$ $\sigma = 15.2$	$\mu = 64.80$ $\sigma = 14.70$	$\mu = 1.54$ $\sigma = 0.90$	$\mu = 7000$
	100	$\mu = 42.60$ $\sigma = 40.30$	$\mu = 82.70$ $\sigma = 15.60$	$\mu = 67.50$ $\sigma = 17.80$	$\mu = 1.53$ $\sigma = 0.74$	$\mu = 5100$
	200	$\mu = 60.00$ $\sigma = 43.70$	$\mu = 85.80$ $\sigma = 14.40$	$\mu = 69.90$ $\sigma = 17.10$	$\mu = 1.45$ $\sigma = 0.58$	$\mu = 3800$
	400	$\mu = 77.90$ $\sigma = 65.00$	$\mu = 82.60$ $\sigma = 18.00$	$\mu = 69.00$ $\sigma = 21.00$	$\mu = 1.56$ $\sigma = 0.93$	$\mu = 4100$
	1200	$\mu = 93.90$ $\sigma = 50.00$	$\mu = 86.60$ $\sigma = 15.00$	$\mu = 77.00$ $\sigma = 18.00$	$\mu = 1.35$ $\sigma = 0.83$	$\mu = 3800$

both UTS and YS. From Figures 18(a) and 18(b), it can be observed that solution treatment for 8 hours for both alloys enhances UTS and YS. In the case of unmodified alloy, the enhancement in strength (UTS and YS) halts with further solution treatment (longer than 8 hours), while a reduction in strength is observed for solution times longer than 50 hours. For the Sr-modified alloy, however, the improvement in strength values continues after solutionizing for 8 hours, reaching

Table 5: Characteristics of Si particles in 413 alloy at different conditions (nonmodified (coded C) and Sr-modified (coded CS) conditions).

Alloy code	Solutionizing time (h)	Particle area (μm^2)	Sphericity (%)	Roundness (%)	Aspect ratio	Density (particles/mm^2)
C	As-cast	$\mu^* = 19.00$ $\sigma^{**} = 19.60$	$\mu = 44.00$ $\sigma = 23.10$	$\mu = 36.60$ $\sigma = 16.70$	$\mu = 3.87$ $\sigma = 1.08$	M = 18000
	8	$\mu = 17.30$ $\sigma = 16.00$	$\mu = 66.90$ $\sigma = 25.10$	$\mu = 50.00$ $\sigma = 22.10$	$\mu = 2.31$ $\sigma = 1.27$	M = 9800
	24	$\mu = 14.90$ $\sigma = 14.80$	$\mu = 74.20$ $\sigma = 20.10$	$\mu = 51.70$ $\sigma = 19.20$	$\mu = 2.10$ $\sigma = 1.03$	M = 8200
	50	$\mu = 27.60$ $\sigma = 19.40$	$\mu = 73.20$ $\sigma = 19.80$	$\mu = 52.50$ $\sigma = 19.00$	$\mu = 2.02$ $\sigma = 0.95$	M = 6300
	100	$\mu = 42.00$ $\sigma = 29.40$	$\mu = 73.50$ $\sigma = 19.00$	$\mu = 52.90$ $\sigma = 18.40$	$\mu = 2.01$ $\sigma = 0.91$	M = 4400
	200	$\mu = 61.50$ $\sigma = 36.80$	$\mu = 74.10$ $\sigma = 18.30$	$\mu = 54.60$ $\sigma = 19.10$	$\mu = 1.99$ $\sigma = 0.90$	M = 3400
	400	$\mu = 72.50$ $\sigma = 35.6$	$\mu = 76.10$ $\sigma = 17.40$	$\mu = 55.2$ $\sigma = 17.10$	$\mu = 1.82$ $\sigma = 0.70$	M = 2800
	1200	$\mu = 91.50$ $\sigma = 31.2$	$\mu = 78.10$ $\sigma = 16.30$	$\mu = 60.40$ $\sigma = 17.30$	$\mu = 1.52$ $\sigma = 0.70$	M = 1900
CS	As-cast	$\mu = 3.59$ $\sigma = 6.28$	$\mu = 52.70$ $\sigma = 23.90$	$\mu = 46.50$ $\sigma = 20.90$	$\mu = 1.96$ $\sigma = 0.78$	$\mu = 34000$
	8	$\mu = 6.11$ $\sigma = 6.59$	$\mu = 72.20$ $\sigma = 18.40$	$\mu = 57.00$ $\sigma = 15.90$	$\mu = 1.69$ $\sigma = 0.60$	$\mu = 18000$
	24	$\mu = 10.50$ $\sigma = 9.99$	$\mu = 75.60$ $\sigma = 18.40$	$\mu = 61.50$ $\sigma = 15.80$	$\mu = 1.56$ $\sigma = 0.56$	$\mu = 10000$
	50	$\mu = 16.50$ $\sigma = 16.00$	$\mu = 79.30$ $\sigma = 18.20$	$\mu = 62.30$ $\sigma = 16.20$	$\mu = 1.56$ $\sigma = 0.53$	M = 7500
	100	$\mu = 36.20$ $\sigma = 24.00$	$\mu = 79.20$ $\sigma = 17.70$	$\mu = 63.40$ $\sigma = 16.50$	$\mu = 1.57$ $\sigma = 0.64$	M = 5400
	200	$\mu = 47.30$ $\sigma = 28.10$	$\mu = 80.30$ $\sigma = 16.10$	$\mu = 64.20$ $\sigma = 14.90$	$\mu = 1.5$ $\sigma = 0.467$	M = 4400
	400	$\mu = 58.30$ $\sigma = 21.2$	$\mu = 82.40$ $\sigma = 16.4$	$\mu = 66.30$ $\sigma = 13.90$	$\mu = 1.5$ $\sigma = 0.467$	M = 3500
	1200	$\mu = 69.30$ $\sigma = 22.10$	$\mu = 85.30$ $\sigma = 15.10$	$\mu = 71.40$ $\sigma = 14.4$	$\mu = 1.5$ $\sigma = 0.467$	M = 3000

maximum values of UTS and YS after solution treatment for 50 hours at 550°C. The strength values begin to deteriorate thereafter for longer periods of solution treatment (i.e., 100, 200, and 400 hours).

The ductility behavior is also similar in the nonmodified, unmodified, and Sr-modified alloys. Ductility values improve significantly after solution treatment for 8 hours at 550°C compared to the ductility values in the as-cast condition for both alloys. The ductility of the unmodified alloy remains constant between 8 and 50 hours of solutionizing, followed by further enhancement to achieve a peak value of 9.7% after 100 hours of solution treatment and remains almost constant up to 200 hours. On the other hand, ductility values of Sr-modified alloy show a continuous enhancement up to 50 hours of solutionizing where the ductility reaches its peak value of 10.5%. The longest duration of solution treatment (i.e., 400 hours) results in reduction in the ductility values of both alloys to about 8%. Figures 18(c) and 18(d) exhibit the shape and distribution of the eutectic Si particles sectioned from a Sr-modified tensile bar solutionized at 550°C for 50 h revealing the difference in 2D (before deep etching) and 3D (same sample after deep etching). As can be seen, due to the collision of the Si particles in Figure 18(d), it is difficult to determine their individual sphericity or the exact particle size (e.g., section A-A or B-B in Figure 18(d)). In addition, the joint particles in Figure 18(d) are not forming a straight line. Therefore, it is also difficult to measure their actual length (thick white broken line). Since the 2D micrographs represent the cross-sections of such particles, they appear nearly spherical which explains the reported high standard deviations in Tables 2–5.

The tensile curves of Al-Si-Cu-Mg 319-type alloys could be divided into four regions across the range of solution temperatures used. This is shown schematically in Figure 19 [29, 30]. Region I corresponds to the change in tensile properties of the alloy on going from the as-cast to the solution heat-treated condition. Region II represents the recommended solution treatment temperature range. Region III represents a continuation of region II until peak properties are reached (spheriodization/coarsening), following which incipient melting begins to occur, while Region IV corresponds directly to the progress of incipient melting with the increase in the solution temperature.

Figure 20 shows the microstructure corresponding to the early stages of incipient melting when the tensile bars are solutionized at a temperature just above region III (520°C) revealing the presence of a large number of pores (Figure 20(a)). Figure 20(b) is a high magnification of

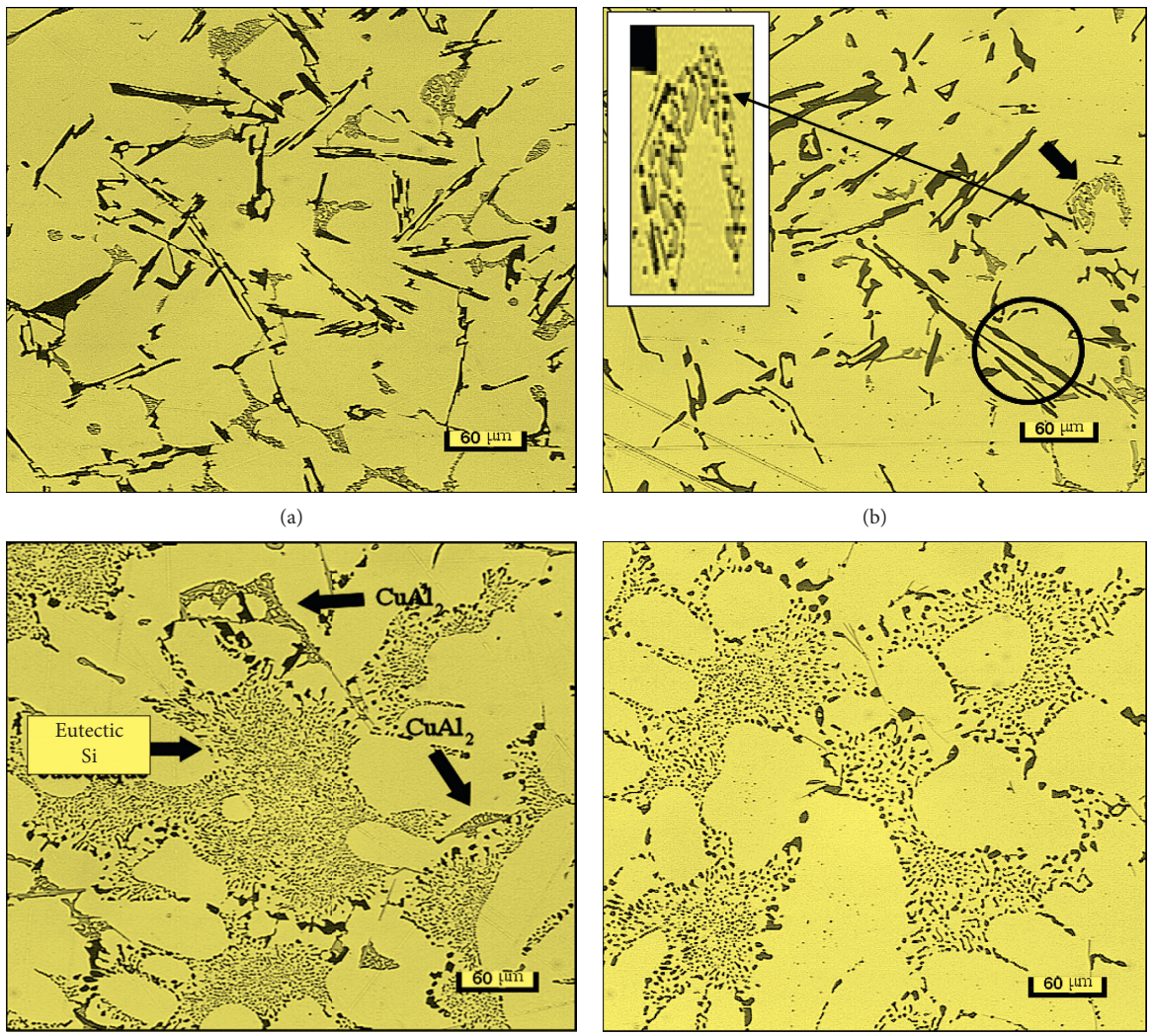

Figure 8: Optical microstructures of 319 alloy: (a) as-cast, (b) SHT for 24 h (fragmentation in black circle), (c) Sr-modified alloy-as-cast, and (d) SHT for 24 h.

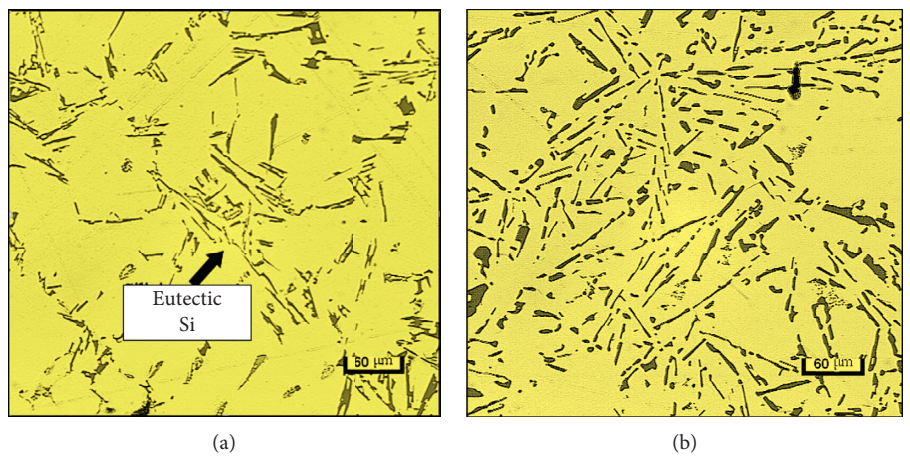

Figure 9: Continued.

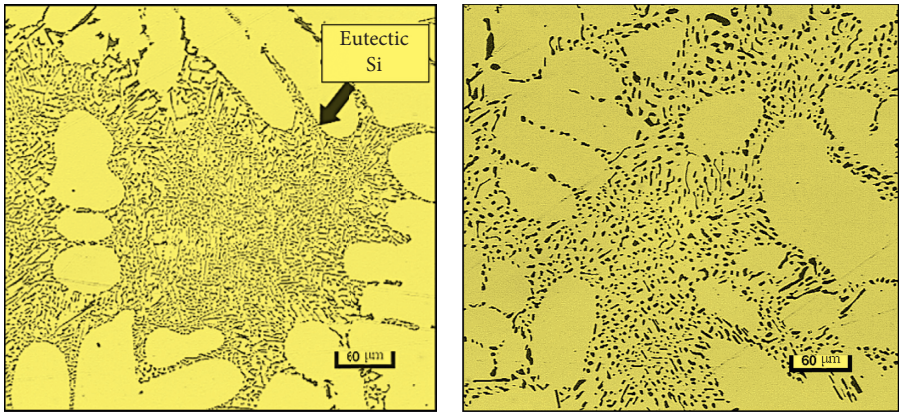

(c) (d)

Figure 9: Optical microstructures of 356 alloy: (a) as-cast, (b) SHT for 24 h, (c) Sr-modified alloy-as-cast, and (d) SHT for 24 h.

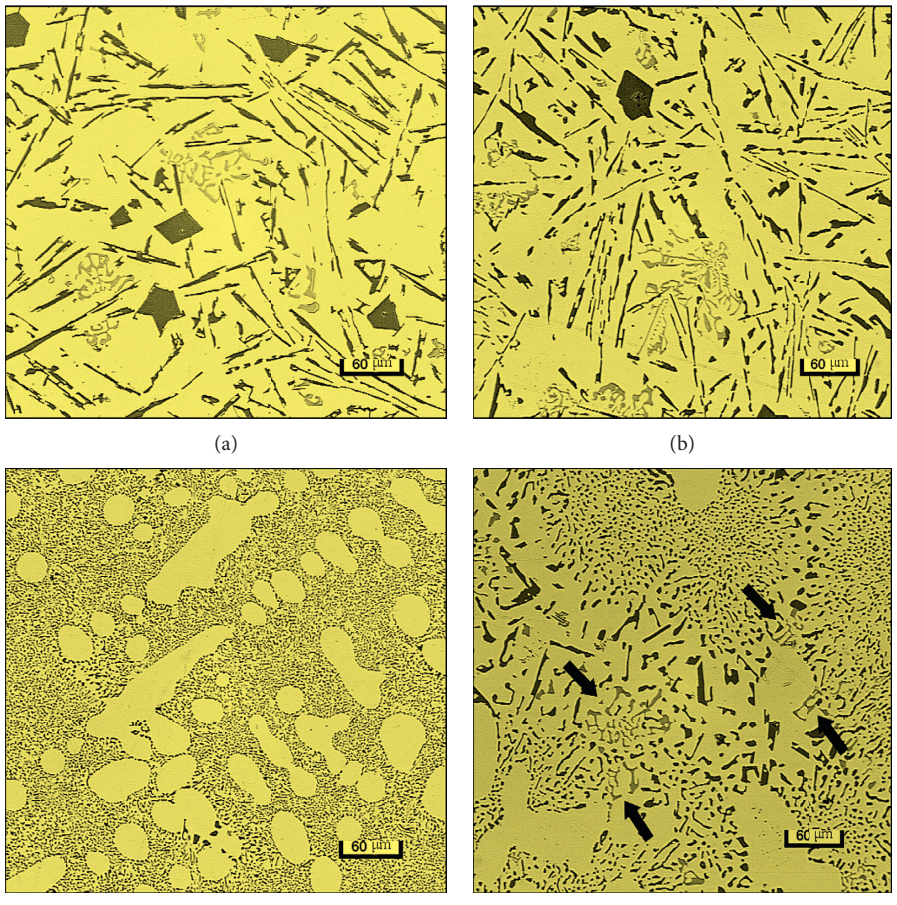

(a) (b)

(c) (d)

Figure 10: Optical microstructure of 413 alloy: (a) as-cast, (b) SHT for 24 h, (c) Sr-modified alloy-as-cast, and (d) SHT for 24 h.

Figure 20(a) displaying the precipitation of thin platelets of π-$Al_8Mg_3FeSi_6$ phase, whereas the white circle clearly displays the presence of some platelets within the pore that was caused due to incipient melting. The details of these platelets are depicted in Figure 20(c).

Figure 21 illustrates the presence of the macrocracks observed in bars of the same alloy as in Figure 20 after solutionizing at 550°C (region IV). This may have occurred because of the severity of the incipient melting. Quenching would also result in localized plastic deformation related to

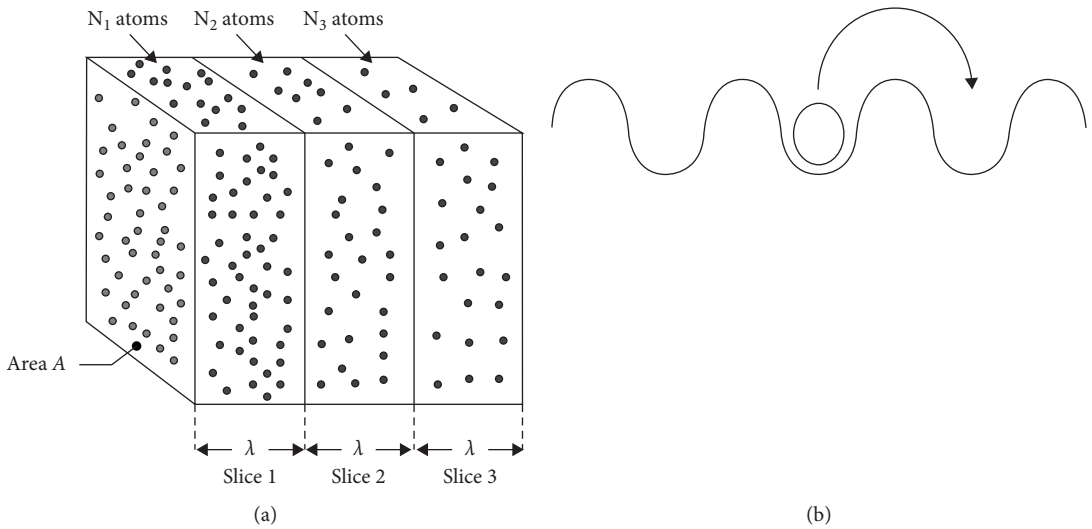

Figure 11: (a) Diffusion from a concentration gradient [25]. (b) Impurity atom diffusing along with a periodic potential [26].

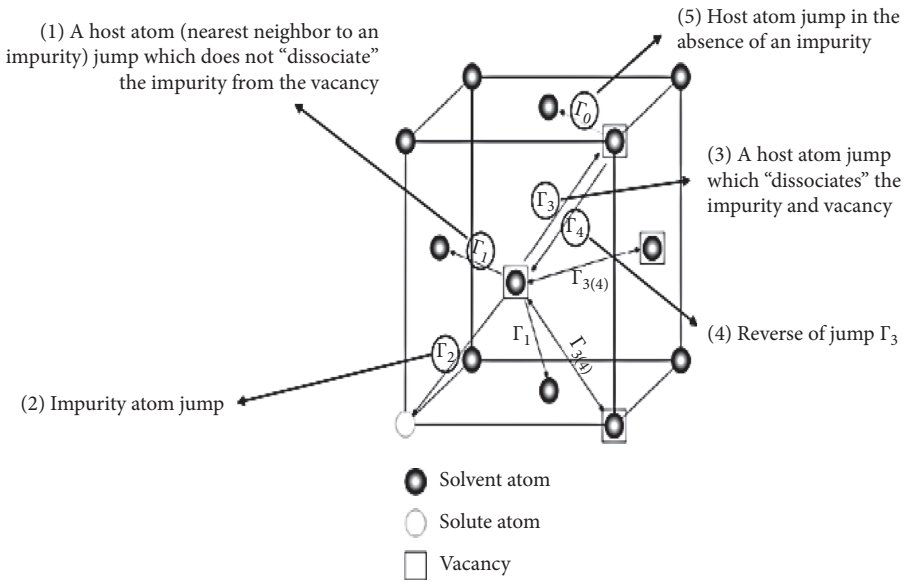

Figure 12: Five frequency model illustration for the case of an fcc system with a dilute impurity concentration. The arrows indicate the direction of the vacancy jump [27].

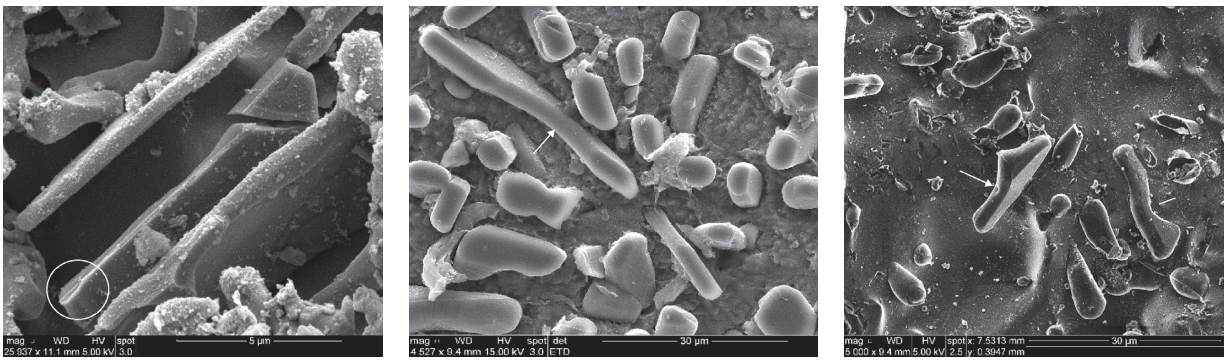

(a) (b) (c)

Figure 13: Continued.

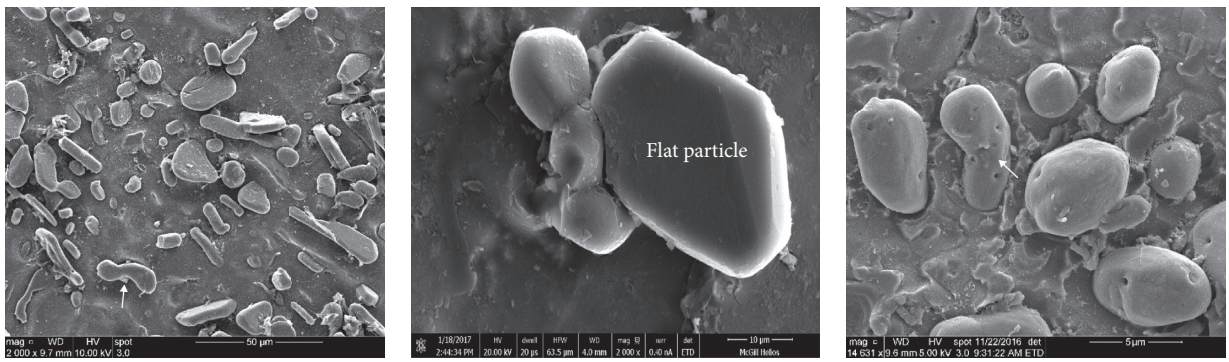

(d) (e) (f)

Figure 13: Changes in the size and distribution of Si particles in nonmodified 356 alloy as a function of heating at 550°C at various times: (a) as-cast, (b) 24 h, (c) 100 h, (d) 400 h, (e) high magnification image of (d), and (f) 1200 h.

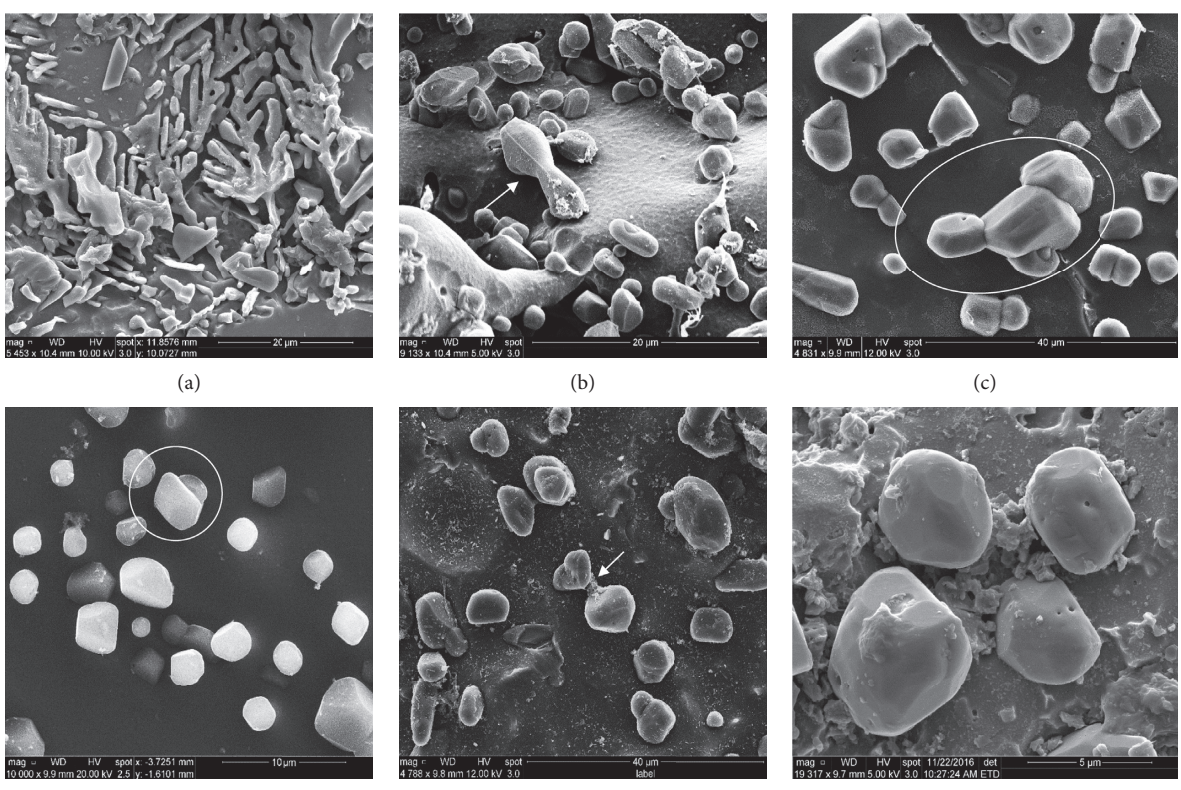

(a) (b) (c)

(d) (e) (f)

Figure 14: Changes in the size and distribution of Si particles in Sr-modified 356 alloy as a function of heating at 550°C at various times: (a) as-cast, (b) 24 h, (c) 200 h, (d) 400 h, (e) 800 h, and (f) 1200 h (white arrows point to necking).

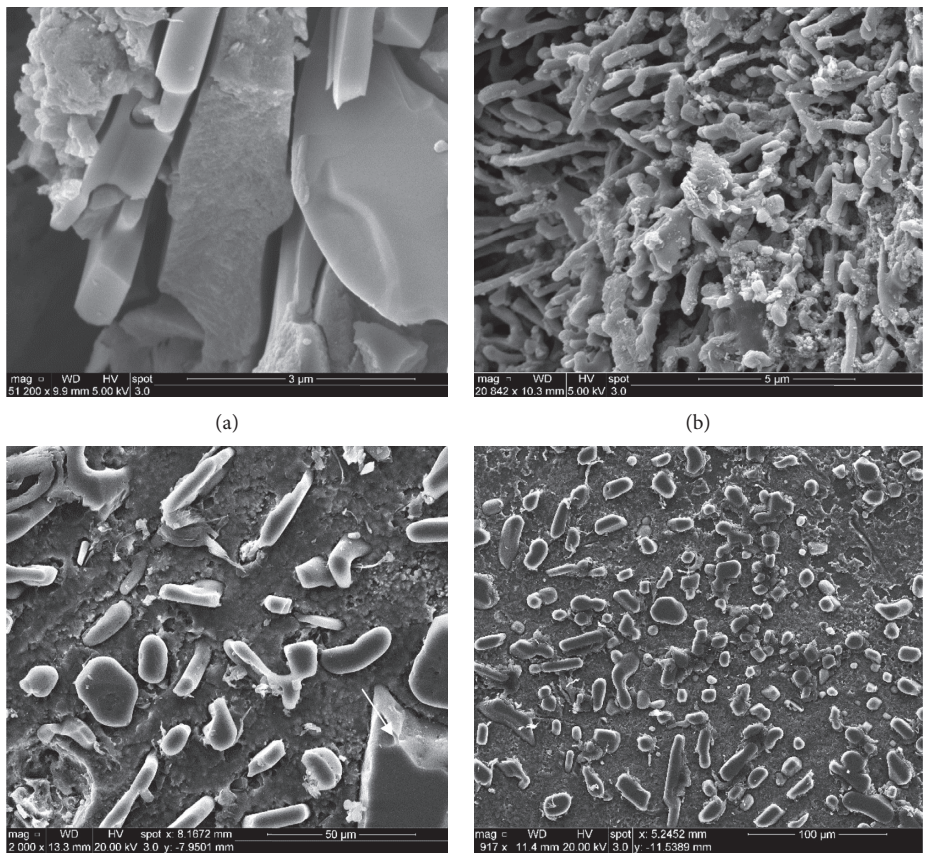

(a) (b)

(c) (d)

Figure 15: Changes in the size and distribution of Si particles in 413 alloy as a function of heating at 510°C at various times: (a) as-cast-unmodified, (b) as-cast-modified, (c) 1200 h, unmodified, and (d) 1200 h, modified.

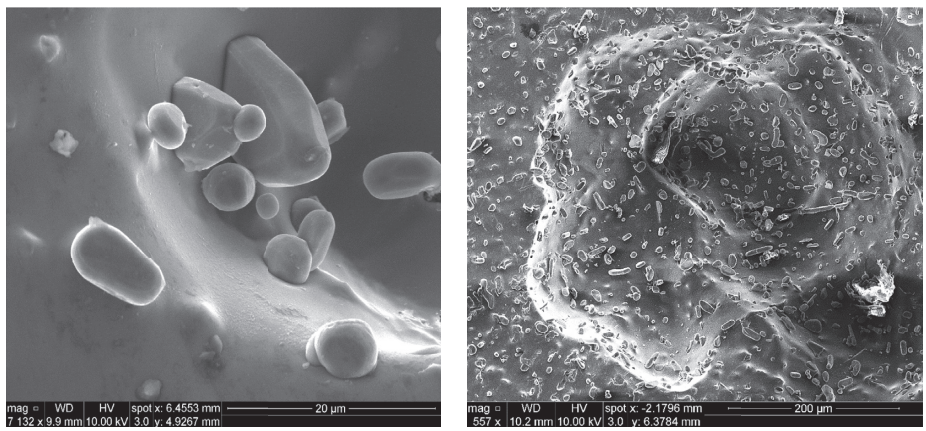

(a) (b)

Figure 16: Incipient melting after SHT for 8 h/565°C in (a) 356 alloy and (b) 413 alloy.

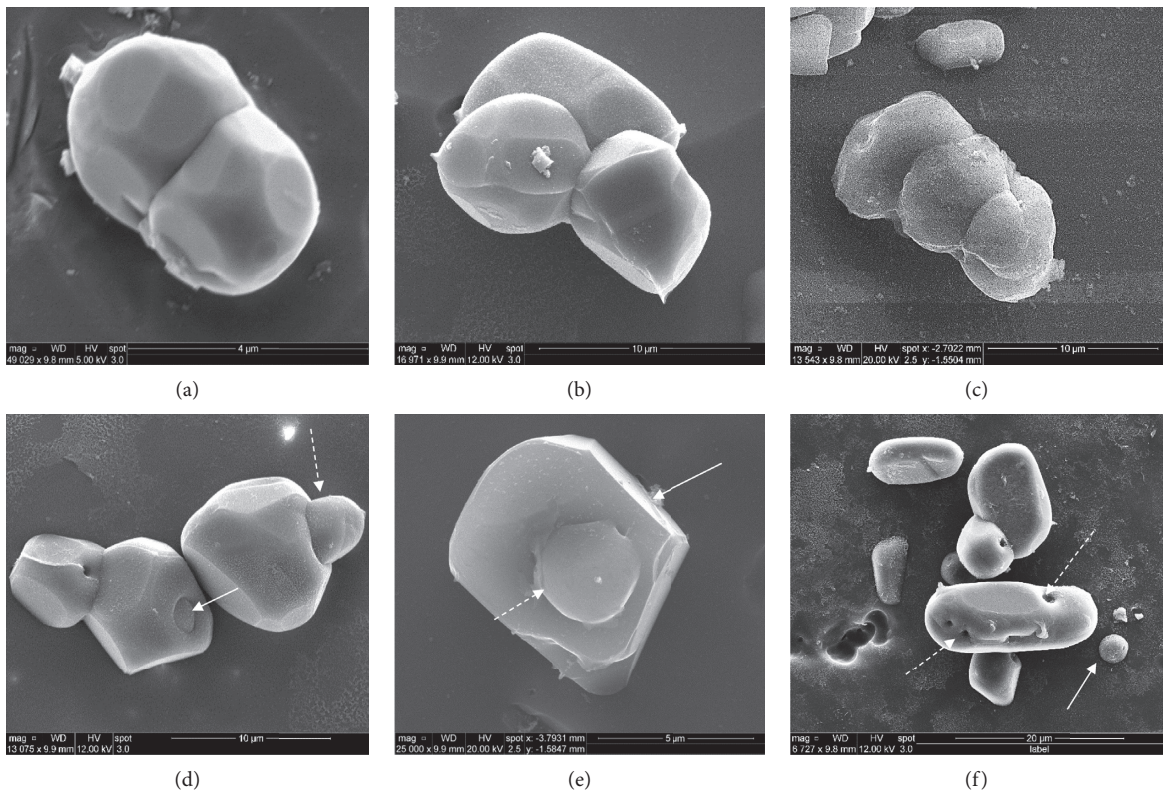

Figure 17: Proposed coarsening processes/mechanisms: (a, b) particle impingement, (c) agglomeration, (d, e) fusion, and (f) dissolution (Ostwald ripening).

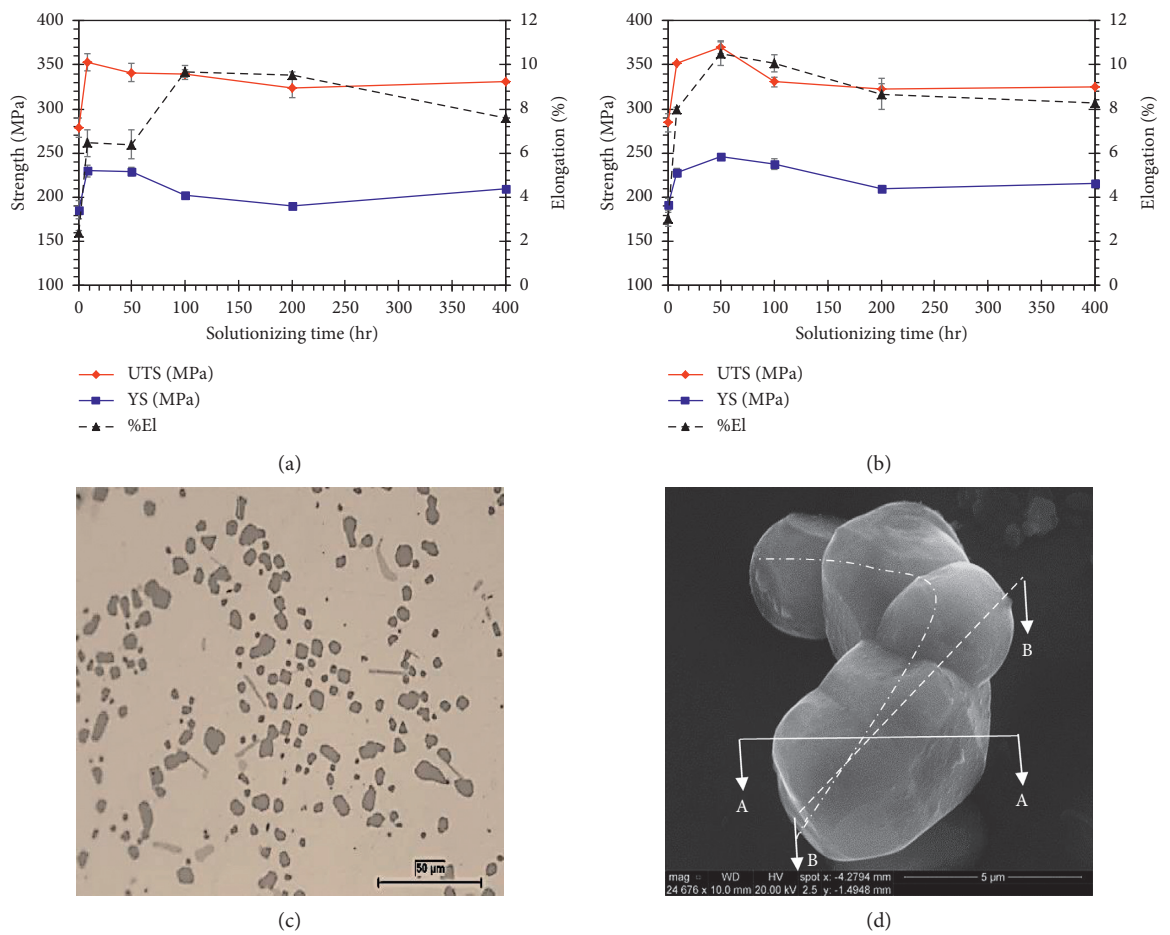

Figure 18: Plots of room temperature tensile properties of 356 alloy in the T4 temper: (a) unmodified alloy; (b) Sr-modified alloy; coarsening of Si particles in Sr-modified alloy after solutionizing at 550°C for 50 h: (c) 2D and (d) 3D.

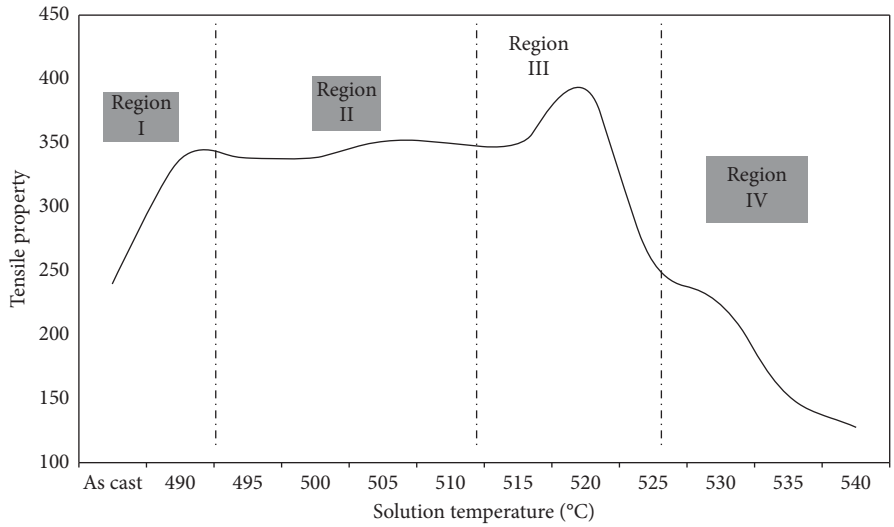

Figure 19: Schematic diagram showing the progress of a tensile property curve as a function of solution treatment temperature [29, 30].

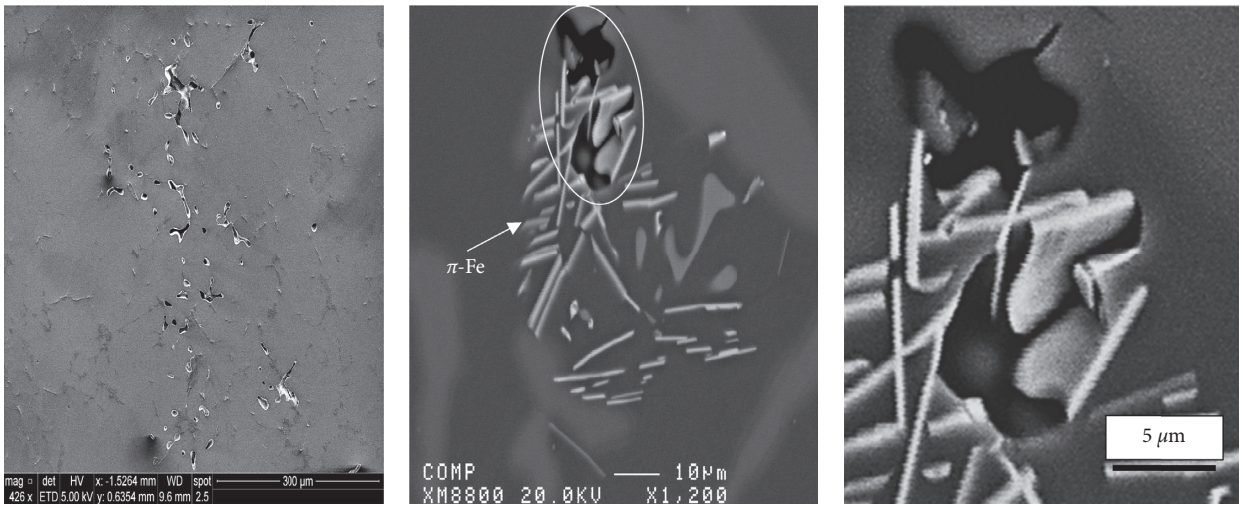

(a) (b) (c)

Figure 20: Backscattered electron images of 319 alloy (with 0.4% Mg) solutionized at 520°C: (a) general view, (b) presence of π–Fe platelets around and inside a pore, and (c) a high magnification electron image of the white circle in (b).

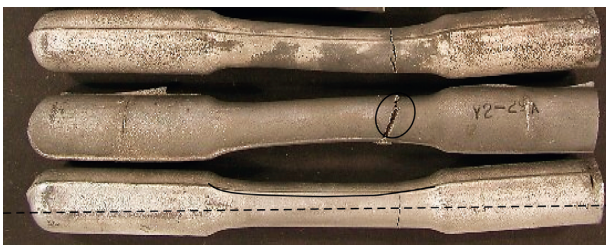

Figure 21: Macrocracking observed in 319 alloy after solutionizing at 550°C (about 40°C above the melting point of Al_2Cu); note the deflection in the last bar (sold black line) under gravity compared to the centre line (broken line) [30].

the transient temperature differences within the bar, establishing a system of residual stresses simultaneously (region IV).

4. Conclusions

Based on the results documented in the present work, the following conclusions may be drawn:

(1) Complete spheroidization of eutectic Si particles in terms of achieving individual spherical particles cannot be obtained in most Al-Si-Cu-Mg alloys even after a solutionizing time of 1200 h which contradicts with the theory of Paray and Gruzleski [14]

(2) Addition of Sr to 356 alloy (Cu-free) could lead to spheroidization after 1200 h/550°C if the alloy is solidified at a high rate, i.e., 8°C/s

(3) Beside the dissolution theory of Ostwald, coarsening of Si particles can as well take place by impingement, fusion, and agglomeration

(4) Increasing the Si content makes it difficult to achieve spheroidization, through fragmentation and coarsening

(5) Results obtained from observation of deeply etched samples (3D) contradict the observations made from polished samples (2D)

Data Availability

The data used to support the findings of this study are available from the corresponding author upon request.

Conflicts of Interest

The authors declare that they have no conflicts of interest.

References

[1] W. Ostwald, "Studies on the formation and transformation of solid bodies," *Zeitschrift für Physikalische Chemie*, vol. 22, pp. 289–330, 1897.

[2] W. Ostwald, "Studies on the formation and transformation of solid bodies," *Journal of Physical Chemistry*, vol. 37, p. 385, 1901.

[3] A. I. Ibrahim, A. M. Samuel, F. H. Samuel, and H. W. Doty, "Response of varying levels of silicon and transition elements on room and elevated temperature tensile properties in an Al-Cu alloy," in *Proceedings of the 122nd Metalcasting Congress*, American Foundry Society, Fort Worth, TX, USA, April 2018.

[4] M. A. Moustafa, F. H. Samuel, and H. W. Doty, "Effect of solution heat treatment and additives on the microstructure of Al-Si (A413.1) automotive alloys," *Journal of Materials Science*, vol. 38, no. 22, pp. 4507–4522, 2003.

[5] C. Meyers, "Solution heat treatment effects on ultimate tensile strength and uniform elongation in A357 aluminum alloys," *AFS Transactions*, vol. 91, pp. 511–518, 1986.

[6] S. Shivkumar, S. Ricci Jr., B. Steenhoff, D. Apelian, and G. Sigworth, "An experimental study to optimize the heat treatment of A356 alloy," *AFS Transactions*, vol. 97, pp. 791–810, 1989.

[7] I. M. Lifshitz and V. V. Slyozov, "The kinetics of precipitation from supersaturated solid solutions," *Journal of Physics and Chemistry of Solids*, vol. 19, no. 1-2, pp. 35–50, 1961.

[8] C. Wagner, "Theorie der Alterung von Niederschlägen durch Umlösen (Ostwald-Reifung)," *Berichte der Bunsengesellschaft für Physikalische Chemie*, vol. 65, no. 7-8, pp. 581–591, 1961.

[9] L. J. Colley, *Microstructure-property models for heat treatment of A356 aluminum alloy*, Ph.D Thesis, University of British Columbia, Vancouver, Canada, 2011.

[10] F. Fracasso, "Influence of quench rate on the hardness obtained after artificial ageing of an Al-Si-Mg alloy," Master Thesis, University of Padova, Padova, Italy, 2010.

[11] B. Parker, "Quantitative evaluation of the microstructure of a strontium-modified Al-Si-Mg alloy following prolonged solution treatment," *Metals Forum*, vol. 5, no. 1, pp. 48–53, 1982.

[12] F. N. Rhines and M. Aballe, "Growth of silicon particles in an aluminum matrix," *Metallurgical Transactions A*, vol. 17, no. 12, pp. 2139–2152, 1986.

[13] D. Apelian, S. Shivkumar, and G. Sigworth, "Fundamental aspects of heat treatment of cast Al-Si-Mg alloys," *AFS Transactions*, vol. 97, pp. 727–742, 1989.

[14] F. Paray and J. Gruzleski, "Modification-a parameter to consider in the heat treatment of Al-Si alloys," *Cast Metals*, vol. 5, no. 4, pp. 187–198, 1993.

[15] B. Forbord, H. Hallem, and K. Marthinsen, "The effect of alloying elements on precipitation and recrystallisation in Al-Zr alloys," *Materials Forum*, 2004.

[16] J. G. Kaufman, *Properties of Aluminum Alloys: Tensile, Creep, and Fatigue Data at High and Low Temperatures*, ASM International, Materials Park, OH, USA, 1999.

[17] E. Ogris, A. Wahlen, H. Lüchinger, and P. J. Uggowitzer, "On the silicon spheroidization in Al-Si alloys," *Journal of Light Metals*, vol. 2, no. 4, pp. 263–269, 2002.

[18] S. Hegde and K. N. Prabhu, "Modification of eutectic silicon in Al-Si alloys," *Journal of Materials Science*, vol. 43, no. 9, pp. 3009–3027, 2008.

[19] H. Li, S. Shivkumar, X. Luo, and D. Apelian, "Influence of modification on the solution heat treatment response of cast Al–Si–Mg alloys," *Cast Metals*, vol. 1, no. 4, pp. 227–234, 1989.

[20] R.-X. Li, R.-D. Li, Y.-H. Zhao, and C.-X. Li, "Effect of heat treatment on eutectic silicon morphology and mechanical property of Al-Si-Cu-Mg cast alloys," *Transactions of Nonferrous Metals Society of China*, vol. 14, no. 3, pp. 496–500, 2004.

[21] J. W. Martin, R. D. Doherty, and B. Cantor, *Stability of Microstructure in Metallic Systems*, Cambridge University Press, Cambridge, UK, 1997.

[22] M. H. Abdelaziz, *Microstructural and mechanical characterization of transition elements-containing Al-Si-Cu-Mg alloys for elevated-temperature applications*, Ph.D Thesis, Université du Québec à Chicoutimi, Saguenay, Canada, 2018.

[23] Z. Li, A. M. Samuel, F. H. Samuel, C. Ravindran, S. Valtierra, and H. W. Doty, "Parameters controlling the performance of AA319-type alloys Part I. tensile properties," *Materials Science and Engineering A*, vol. 367, no. 1-2, pp. 96–110, 2004.

[24] Z. Li, A. M. Samuel, F. H. Samuel, C. Ravindran, H. W. Doty, and S. Valtierra, "Parameters controlling the performance of AA319-type alloys Part II. impact properties and fractography," *Materials Science and Engineering A*, vol. 367, no. 1-2, pp. 111–122, 2004.

[25] C.-L. Chen, A. Richter, and R. C. Thomson, "Investigation of mechanical properties of intermetallic phases in multi-component Al-Si alloys using hot-stage nanoindentation," *Intermetallics*, vol. 18, no. 4, pp. 499–508, 2010.

[26] T. I. Kamins, J. Manoliu, and R. N. Tucker, "Diffusion of impurities in polycrystalline silicon," *Journal of Applied Physics*, vol. 43, no. 1, p. 83, 1972.

[27] A. D. LeClaire and A. B. Lidiard, "Statistical theories of atomic transport in crystalline solids," *Philosophical Magazine*, vol. 47, p. 518, 1970.

[28] K. Nogita, S. D. McDonald, and A. K. Dahle, "Modification of Al-Si alloys," Edited by J. F. Nie, A. J. Morton, and B. C. Muddle, Eds., Institute of Materials Engineering Australasia Ltd, Melbourne, Australia, 2004.

[29] F. H. Samuel, "Incipient melting of $Al_5Mg_8Si_6Cu_2$ and Al_2Cu intermetallics in unmodified and strontium-modified Al-Si-Cu-Mg (319) alloys during solution heat treatment," *Journal of Materials Science*, vol. 33, no. 9, pp. 2283–2297, 1998.

[30] A. M. A. Mohamed, F. H. Samuel, and S. Al kahtani, "Influence of Mg and solution heat treatment on the occurrence of incipient melting in Al-Si-Cu-Mg cast alloys," *Materials Science and Engineering: A*, vol. 543, pp. 22–34, 2012.